Ventura-Meinersen et al. *EPJ Quantum Technology* (2025) 12:125
https://doi.org/10.1140/epjqt/s40507-025-00426-2

EPJ Quantum Technology
a SpringerOpen Journal

RESEARCH Open Access

Quantum geometric protocols for fast high-fidelity adiabatic state transfer

Chris Ventura-Meinersen[1*], Stefano Bosco[1] and Maximilian Rimbach-Russ[1]

*Correspondence:
[1]QuTech and Kavli Institute of Nanoscience, Delft University of Technology, PO Box 5046, 2600 GA Delft, The Netherlands

Abstract

Efficient adiabatic control schemes, where one steers a quantum system along an adiabatic path ensuring minimal excitations while achieving a desired final state, that enable fast, high-fidelity operations are essential for any practical quantum computation. However, current optimization protocols are not universally tractable due to stringent requirements imposed by the microscopic systems encoding the qubit, including complex energy level structures and unwanted transitions, and generally require a trade-off between speed and fidelity of the operation. Here, we address these challenges by developing a general framework for optimal control based on the quantum metric tensor. This framework allows for fast and high-fidelity adiabatic pulses, even for a dense energy spectrum, based solely on the Hamiltonian of the system instead of the time evolution propagator and independent of the size of the underlying Hilbert space. Furthermore, our framework suppresses diabatic transitions and state-dependent crosstalk effects without the need for additional control fields. As an example, we study the adiabatic charge transfer in a double quantum dot to find optimal control pulses with improved performance. We show that for the geometric protocol, the transfer fidelities are lower bounded $\mathcal{F} > 99\%$ for ultrafast 20 ns pulses, regardless of the size of the anti-crossing, while being robust against miscalibration errors and quasistatic noise.

Keywords: Optimal quantum control; Quantum geometry; Adiabatic state transfer; Spin qubits; Semiconductor quantum dot qubits; Quantum computing

Coherent control of quantum information is the central part of the advancement of emerging quantum technologies such as quantum processors, quantum sensors, and quantum communication [1]. However, the inherently fragile nature of quantum states makes their coherent control a challenging task. Much research is dedicated to finding so-called quantum optimal control protocols, that allow fast and high-fidelity operations by appropriately shaping the control pulses [1–6]. Optimized initialization and readout protocols are of particular interest, as they are an integral part of any error correction algorithm [7].

Optimal control protocols can be roughly divided into three main categories. Firstly, there are geometric approaches that rewrite the time evolution into Pontryagin's Maximum Principle [8–16]. Extensions of the geometric protocols also intend to circumvent incoherent dynamics [12, 17–20]. Secondly, fully numerical techniques, such as the

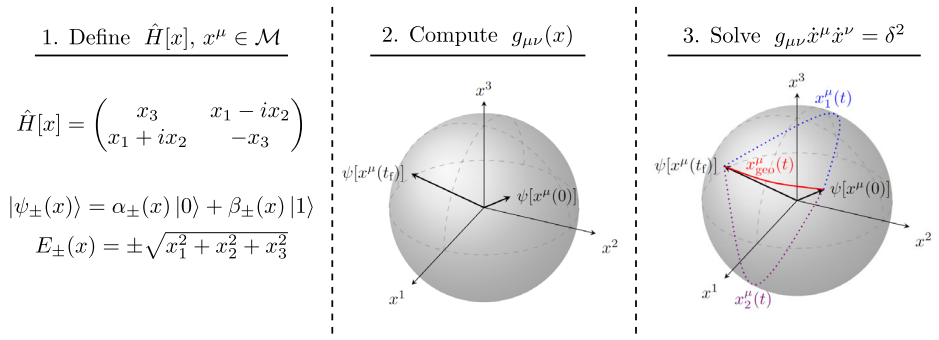

Figure 1 Schematic representation of the geometric fast-QUAD approach for a single qubit. First, one defines the system Hamiltonian and the respective parameters $x^\mu = (x^1, x^2, x^3)$ one wants to optimally operate. The number of parameters defines the dimension of the quantum metric tensor $g_{\mu\nu}$. For a qubit Hamiltonian, the underlying parameter manifold is the Bloch sphere. The geodesic on the sphere (red line) gives the optimal path connecting two states. Examples of non-optimal state transfer protocols (x_1^μ, x_2^μ) are drawn as blue and purple, dotted lines

GRAPE [21, 22] and CRAB algorithms [23, 24], can be used to find a (hopefully) global minimum of the error by varying parameters of the input signal. As these protocols are based on classical optimization problems, they come at the cost of the computational overhead and flexibility to small modifications, often limiting them to smaller problem sizes. Lastly, inherent error suppression can be achieved via (enforced) adiabatic dynamics [4, 17, 25–43]. However, often the suppression of additional transitions is generically forced through the control of new components of the driving Hamiltonian like in the transitionless driving method [27, 37], which may be experimentally inaccessible. Approximate methods circumvent these additional control fields and only affect the experimentally accessible parameters while providing fast and quasiadiabatic (fast-QUAD) protocols [40, 44–46].

In this work, we develop a geometric framework, making use of the benefits of the first and last class, based on geodesics in the space provided by the quantum metric tensor [47–52]. Furthermore, our framework can be generalized to any multi-level Hamiltonian and allows for fast and high-fidelity adiabatic operations without needing the computational overhead akin to the numerical approaches. We refer to this approach as the *geometric fast-QUAD*. Our geometric fast-QUAD does not require imposing any new external control fields, is resistant to miscalibration errors, allows for fast operations even in dense energy landscapes, and does not require the computation of the full time-ordered evolution operator. It reduces undesired level transitions and initialization, and readout-induced crosstalk by traversing rapidly through regions of charge uncertainties [53]. In addition, our framework can be easily adapted to account for different quantum operations [54] and can be efficiently extended to large-size systems [55]. We show the advantages of the geometric fast-QUAD through an optimal protocol for initialization and readout of semiconductor spin-qubits.

Semiconductor spin qubits are a platform for quantum computing based on confined semiconductor quantum dots with a promise to be scalable [56, 57], with long coherence times [58], operability at high temperatures [59, 60], and their similarity in fabrication to the classical semiconductor industry [61–63]. However, their small size can lead to dense energy spectra that may hinder fast and high-fidelity quantum control. For read-

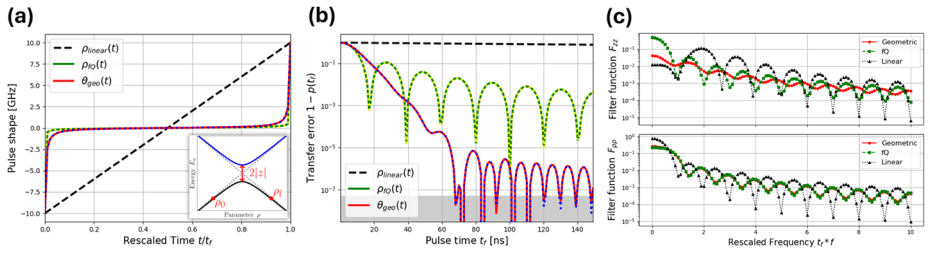

Figure 2 Comparison of coherent qubit state transfer. **(a)** shows the linear (black, dashed), standard fast-QUAD (analytic solution from [46] in green, numerical solution in yellow), and geometric fast-QUAD (analytic solution in red, numerical in blue) pulse shapes. In addition, the inset shows energy levels as a function of ρ. We find that the standard fast-QUAD leads to a sharper pulse shape requiring high bandwidth. In **(b)**, we plot the respective transfer error $1 - p(t_f) = 1 - |\langle\psi_0(t_f)|\psi(t_f)\rangle|^2$ as a function of pulse time t_f. As the quantum metric tensor (9) is independent of ϕ we can choose a protocol exclusively for $\rho(t)$ or for the ratio $\theta(t) = \arctan2(\rho(t), z(t))$. Using the quantum adiabatic protocol (4) we find analytically that $\theta_{\text{geo}}(t) = (\theta_f - \theta_0)\, t/t_f + \theta_0$, where the adiabaticity is given by the ramp rate $\delta = (\theta_f - \theta_0)/t_f$. Throughout these simulations the values of $\phi = 0$, $\rho_0 = -10$ GHz, $\rho_f = 10$ GHz, $z = 0.1$ GHz have been used. Note that the precision of the numerical simulations determines the singular behavior (gray area) in the transfer error. The geometric fast-QUAD consistently outperforms the linear and the standard fast-QUAD after 20 ns if we exclude the resonance. We note that the use of such resonances is limited in realistic scenarios with a finite bandwidth and time precision [42]. **(c)** We show the filter functions for noise acting both in the direction of the control parameter $F_{\rho\rho}$ and in the direction of the other parameter F_{zz}. The filter functions, defined in Eq. (11), describe the extent to which any given pulse shape overlaps with an arbitrary noise spectral density and hence quantify its exposure to it [68]. Here, we study the rescaled pulse shapes $\rho(t)/z$, and we find that the geometric fast-QUAD is resilient in the low-frequency regime to noise acting on any parameter, while the standard fast-QUAD is only resilient in the direction of the control parameter. The linear pulse shows a strongly oscillatory behavior, making it difficult to predict its noise susceptibility

ing out and initializing such qubits, the measured signal is typically enhanced through spin-to-charge conversion techniques [64, 65]. Common spin-to-charge techniques, such as Pauli-Spin-Blockade (PSB), rely on an adiabatic transition between a spin and a charge state [66] passing through multiple anticrossings. We illustrate the advantages of the geometric fast-QUAD by optimizing the PSB initialization and readout in a double quantum dot (DQD) with experimentally feasible parameters. Furthermore, we expand on previous results in [40, 46] by including the theoretical framework based on quantum geometry, allowing for generalized pulse engineering in multi-parameter Hamiltonians robust against miscalibration errors and quasistatic noise.

The article is structured as follows. First, the general framework is introduced, starting with the geometric formalism, relating optimal protocols to geodesics, and applying it to a general qubit Hamiltonian. Subsequently, upon reviewing the general DQD model in the presence of strong spin-orbit interaction [67], an effective three-level Hamiltonian, describing the readout and initialization subject to PSB, is introduced and analyzed under unitary and non-unitary evolution using the geometric fast-QUAD and compared to the linear and standard fast-QUAD methods. In addition, we provide a detailed analysis of the robustness of the geometric fast-QUAD under quasistatic noise and miscalibration errors.

1 Results

1.1 Quantum geometric formalism: fast-quasiadiabatic dynamics as geodesics

Optimal control schemes rely on the control of parameters $x^\mu = (x^1, x^2 \ldots, x^n)$ of the physical Hamiltonian $H[x^\mu]$ to provide high-fidelity state transfer. The task of optimizing the fidelity of state transfer $|\psi(x)\rangle \to |\psi(x')\rangle$ can be captured by the parameter space trajectory $x \to x'$ through the geometry described by the quantum metric tensor (See [48] for a

review). The quantum metric tensor $g_{\mu\nu}$ describes the infinitesimal distance between two pure states via the local infidelity (up to second order in parameter changes) [49, 69]

$$1 - |\langle\psi(x)|\psi(x+dx)\rangle|^2 \approx \frac{1}{2} g_{\mu\nu}(x) dx^\mu dx^\nu. \tag{1}$$

Here, $x^\mu \in \mathcal{M}$, where $\mathcal{M}$ is the set of all possible parameter values, define a set of parameters that define an embedding for the set of pure states $P(\mathcal{H}) = \mathcal{H}/U(1)$. For Greek indices, we will opt for the Einstein summation convention. The quantum metric tensor constitutes the real and symmetric part of the full quantum geometric tensor $q_{\mu\nu} = g_{\mu\nu} + i\Omega_{\mu\nu}$, whose antisymmetric component $\Omega_{\mu\nu}$ is related to the Berry curvature, which captures topological effects [70–73] allowing for a possibility to straightforwardly connect quantum dynamics and topology. For approximately adiabatic dynamics [69], the quantum metric tensor, with respect to a given target state $|\psi_0\rangle$, can conveniently be written in terms of the Hamiltonian $\hat{H}$, its eigenvalues E_n, and eigenvectors $\{|\psi_n\rangle\}$ (See Methods 3.1)

$$g_{\mu\nu} = \mathrm{Re} \sum_{n\neq 0} \frac{\langle\psi_0|\partial_\mu \hat{H}|\psi_n\rangle \langle\psi_n|\partial_\nu \hat{H}|\psi_0\rangle}{(E_n - E_0)^2} = \mathrm{Re}\, q_{\mu\nu}, \tag{2}$$

where $\partial_\mu = \partial/\partial x^\mu$ is the derivative with respect to the parameters of the Hamiltonian. The quantum metric tensor $g_{\mu\nu}$ is a frame-independent object, as opposed to the works in [74, 75], and allows us to connect fast and quasi-adiabatic (fast-QUAD) dynamics with the geometry of the parameter space. For coherent population transfer, experimentally controlled parameters can be written as $x^\mu(t)$. State transfer is then given by a path connecting the set of initial parameter values $x^\mu_{\mathrm{i}} \equiv x^\mu(0)$ to some final set $x^\mu_{\mathrm{f}} \equiv x^\mu(t_{\mathrm{f}})$. The task of fast and high-fidelity population transfer then relates to the optimization problem of finding an optimal path $x^\mu_{\mathrm{geo}}(t)$ between these two points described by the following functional

$$\mathcal{L}[x, \dot{x}] = \int_0^{t_{\mathrm{f}}} dt \sqrt{g_{\mu\nu}(x) \frac{\mathrm{d}x^\mu}{\mathrm{d}t} \frac{\mathrm{d}x^\nu}{\mathrm{d}t}}. \tag{3}$$

This functional describes the length of a path $x^\mu(t)$ parametrized by time t and can be minimized for functions $x^\mu_{\mathrm{geo}}(t)$ (See Fig. 1) that solve the Euler-Lagrange equations, which in this context are known as the geodesic equations. Note that we can always add a constraint functional $\mathcal{C}[x, \dot{x}]$, altering the equations of motion in parameter space (See Methods 3.2). For adiabatic protocols, the geodesics fulfill the geometric-adiabatic condition (See Methods 3.1)

$$g_{\mu\nu}(x) \frac{\mathrm{d}x^\mu}{\mathrm{d}t} \frac{\mathrm{d}x^\nu}{\mathrm{d}t} = \delta^2 \ll 1. \tag{4}$$

For now, δ is a constant parameter ensuring the boundary conditions for the pulse. Since the above relationship minimizes the local infidelity (1), the geodesics also minimize the energy fluctuations [76]

$$\sigma_E^2 = \left\langle \hat{H}^2 \right\rangle - \left\langle \hat{H} \right\rangle^2 \propto g_{\mu\nu}(x) \frac{\mathrm{d}x^\mu}{\mathrm{d}t} \frac{\mathrm{d}x^\nu}{\mathrm{d}t}. \tag{5}$$

Hence, we see that, for adiabatic evolution, our geometric fast-QUAD directly minimizes the main coherent error, namely, diabatic excitations (See Methods 3.3). As $\delta^2 \propto \sigma_E^2$, we call δ the adiabaticity since it is equal to the energy standard deviation. If we restrict ourselves to a single parameter $x^\mu = \varepsilon(t)$, we can solve for the adiabaticity parameter as follows

$$\delta = \frac{1}{t_\mathrm{f}} \int_{\varepsilon(0)}^{\varepsilon(t_\mathrm{f})} d\varepsilon \, \sqrt{g_{\varepsilon\varepsilon}} = \frac{\mathcal{L}[\varepsilon]}{t_\mathrm{f}} \ll 1. \tag{6}$$

Therefore, adiabatic protocols can be understood as paths that minimize locally the length of the path that they trace out, i.e. short geodesics with respect to the time t_f. This relationship can also be extended to the multi-parameter case by substituting Eq. (4) into Eq. (3). From the perspective of adiabatic perturbation theory, we can then see the quantum metric tensor as minimizing the first-order non-adiabatic transitions. The above equation also converges to the quantum speed limit bound for pure states as found in [76]. Finally, this allows us to draw a connection between adiabatic dynamics and geometry. To find an optimal time evolution of $\varepsilon(t)$, we need to solve

$$g_{\varepsilon\varepsilon}\dot{\varepsilon}^2 = \sum_{n\neq 0} \frac{|\,\langle\psi_0|\partial_\varepsilon \hat{H}|\psi_n\rangle\,|^2}{(E_n - E_0)^2} \left(\frac{\mathrm{d}\varepsilon}{\mathrm{d}t}\right)^2 = \delta^2. \tag{7}$$

Unsurprisingly, this is similar to the known fast-QUAD equation [44–46], differing from the standard fast-QUAD equation only by an additional exponent of 2 of the energy splitting in the denominator [77]. However, our geometric protocols allows for a clear extension to multiple optimization parameters by solving the multi-parameter geodesic equation. In the remainder of the article, we refer to Eq. (7) as *geometric fast-QUAD* equation, which is an explicit expression of Eq. (4) using a single control parameter $\varepsilon(t)$. As boundary conditions, we use Eq. (6) that relates the pulse time to the energy fluctuations. Solving this ordinary differential equation with respective boundary conditions gives our control pulse (See Methods 3.4).

The geometric structure of Hilbert space allows us to optimize adiabatic population transfer. For instance, a two-level Hamiltonian in cylindrical coordinates (ρ, ϕ, z)

$$\hat{H}_\mathrm{Pauli} = \begin{pmatrix} z & \rho\, e^{-i\phi} \\ \rho\, e^{i\phi} & -z \end{pmatrix}, \tag{8}$$

leads to the quantum metric tensor resembling the Bloch sphere (see Methods 3.1)

$$[g_{\mu\nu}(\theta,\phi)] = \frac{1}{4}\begin{pmatrix} 1 & 0 \\ 0 & \sin^2\theta \end{pmatrix}. \tag{9}$$

Here $\theta = \arctan2(\rho, z)$ describes the azimuthal angle of the Bloch sphere. Figure 2 shows the simulated probability $p(t_\mathrm{f}) = |\,\langle\psi_0(t_\mathrm{f})|\psi(t_\mathrm{f})\rangle\,|^2$ under coherent evolution for the linear protocol $\rho_\mathrm{linear}(t) = (\rho_\mathrm{f} - \rho_0)\, t/t_\mathrm{f} + \rho_0$, the standard fast-QUAD, and the geometric protocol as defined in Eq. (4). Using Eq. (4) we find analytically that [78, 79]

$$\theta_\mathrm{geo}(t) = (\theta_\mathrm{f} - \theta_0)\, t/t_\mathrm{f} + \theta_0, \tag{10}$$

where θ_0, θ_f are the initial and final values of $\theta(t)$. For the (geometric) fast-QUAD, we also simulate the pulses numerically to inspect their applicability when analytic methods do not suffice (shown as blue and yellow dashed lines). In both cases, because of the minimization of the energy fluctuations, the transfer errors arising from undesired diabatic transitions are drastically reduced with respect to the linear protocol. The geometric fast-QUAD, however, provides a more stable performance for a wider range of possible pulse times. This robustness can also be seen in Fig. 2 (c), where we plot the filter functions for each pulse for noise acting in the direction of the control parameter $F_{\rho\rho}$ or the other parameter F_{zz}, which describe the extent to which any given pulse is exposed to different parts of the frequency noise spectrum [68]. For a noise Hamiltonian $\hat{H}_{\text{noise}} = \sum_j \delta\lambda_j \sigma_j$ we find that the decoherence decay rate $\chi(t_f)$, up to second order in $\delta\lambda$ and only taking auto-correlations into account, is given by [57, 68, 80, 81]

$$\chi(t_f) = \int_0^\infty \frac{df}{2\pi} \sum_j S_{jj}(f) F_{jj}(f, t_f) \text{ with} \tag{11}$$

$$S_{jj}(f) = 2\int_{-\infty}^{\infty} dt\, \langle \delta\lambda_j(0)\, \delta\lambda_j(t)\rangle \cos\left(2\pi f t\right) \tag{12}$$

$$F_{jj}(f, t_f) = \frac{1}{4}\left|\int_0^{t_f} dt\, \text{tr}\left(U_c^\dagger \sigma_j U_c \sigma_j\right) e^{i2\pi f t}\right|^2, \tag{13}$$

where $U_c(t)$ is the time evolution operator associated to the control pulse. We find that the geometric fast-QUAD is more resilient to low-frequency noise independent of the direction of the noise, which remarks the robustness of the geodesics to small perturbations. Contrary to this, the standard fast-QUAD is only resilient against noise in the control parameters direction. The linear protocol shows a strongly oscillatory behavior with an envelope similar or worse than the other protocols, as seen in Fig. 2 (b). Additionally, the geometric fast-QUAD pulse shape is a smoother function of time and hence reduces the requirements on the control electronics. Moreover, the geometric fast-QUAD can be easily extended to an arbitrary multi-level system, as illustrated in Eq. (2). On the one hand, the quantum metric tensor extrinsically scales with the number of control parameters and is hence also useful for large systems, making it a reliable tool for analyzing and optimizing large-scale quantum architectures. On the other hand, to actually compute it, one needs to sum over different energy eigenstates and eigenenergies, whose computation does scale with the Hilbert space. However, for any given multi-qubit adiabatic state transfer, one can restrict oneself to the subset of eigenenergies and eigenvectors that are closest to the target state. This subset will have the biggest impact on the state transfer fidelity and is, hence, efficiently computable. Furthermore, the enforced adiabaticity makes the generation of the instantaneous eigenstates very efficient as previous time-steps can be used for iterative algorithms such as Filtered Eigensolver Algorithm for Symmetric Targets (FEAST) [82] and Locally Optimal Block Preconditioned Conjugate Gradient (LOBPCG).

1.2 Optimal control of spin-to-charge conversion in a double quantum dot

Given the advantages of the quantum metric tensor, we aim to apply the geometric fast-QUAD for the adiabatic spin-to-charge conversion, which is the important component of initialization and readout processes in spin qubit systems. We study an effective model for a double quantum dot (DQD) system that may be used directly for the initialization

and readout of singlet-triplet qubits [65, 83–86], which currently suffer from initialization and readout errors from coherent and non-unitary sources as seen explicitly in [83]. After providing a brief overview of the microscopic model below, we investigate a truncated two-level model of the full model to extend the previous result of a two-level Landau-Zener problem to one in the presence of $S-T_-$ coupling [83, 84, 87]. Following, we will introduce a low-dimensional effective DQD model, which captures the spin-to-charge transition, while taking into account the spin state. Using this model, we will aim to provide a detailed analysis and comparison of the geometric fast-QUAD with the linear and standard fast-QUAD protocols under coherent and non-unitary errors. In the remaining text, we will work in units of $\hbar$. The results in the single qubit case (Fig. 2) can be extended to the full 6x6 DQD [88, 89], consisting of two spins in the lowest orbitals of two quantum dots. The Hamiltonian is a sum of the Fermi-Hubbard Hamiltonian and the Zeeman Hamiltonian

$$\hat{H}_{\mathrm{DQD}} = \hat{H}_{\mathrm{FH}} + \hat{H}_{\mathrm{Zeeman}}, \tag{14}$$

where the spin-degenerate part is described by the Fermi-Hubbard model

$$\hat{H}_{\mathrm{FH}} = -\Omega \sum_{ij,\sigma} \left(\hat{c}^{\dagger}_{i,\sigma} \hat{c}_{j,\sigma} + \mathrm{h.c.} \right) + \sum_{\langle ij \rangle} U_{ij} \hat{n}_i \hat{n}_j + \sum_j \left(\frac{U}{2} \hat{n}_j (\hat{n}_j - 1) + V_j \hat{n}_j \right) \tag{15}$$

where $\hat{c}^{\dagger}_{j,\sigma}$ ($\hat{c}_{j,\sigma}$) creates (annihilates) a fermion on sites j with spin σ. The fermionic number operator is $\hat{n}_j = \sum_\sigma \hat{c}^{\dagger}_{\sigma,j} \hat{c}_{\sigma,j}$, U and U_{ij} are the intra- and inter-dot Coulomb repulsion, Ω is the tunnel coupling originating from the overlap of the wavefunctions in nearby quantum dots, and V_i are the chemical potentials in each dot. The spin degeneracy is lifted through the Zeeman term

$$\hat{H}_{\mathrm{Zeeman}} = \frac{1}{2} \mu_B \sum_j \vec{\mathcal{B}}^j \cdot \vec{\sigma}^j, \tag{16}$$

where μ_B is the Bohr magneton, $\vec{\sigma} = (\sigma_x, \sigma_y, \sigma_z)^T$ is the Pauli vector consisting of the conventional Pauli matrices, $\mathcal{B}^j_a = \sum_b \mathcal{G}^j_{ab} B_b$ the effective magnetic field and $\mathcal{G}^j_{ab}$ the g-tensor at site j. The indices $a, b = x, y, z$ run over the spatial components. Additionally, we define $E_a = E_{a,1} + E_{a,2}$ and $\Delta E_a = E_{a,1} - E_{a,2}$ as the total Zeeman energy and the Zeeman splitting difference, which may arise due to a spatially varying g-factor as usually found in germanium-based platforms [87, 90–94] or a magnetic field gradient as appears in silicon-based architectures with an additional micromagnet [66, 95–97]. The matrix representation of the double quantum dot Hamiltonian is given by [88, 89]

$$\hat{H}_{\mathrm{DQD}} = \begin{pmatrix} \tilde{U} + \varepsilon & 0 & 0 & -\Omega & \Omega & 0 \\ 0 & \tilde{U} - \varepsilon & 0 & -\Omega & \Omega & 0 \\ 0 & 0 & E_Z & \Delta E_X & -\Delta E_X & 0 \\ -\Omega & -\Omega & \Delta E_X & \Delta E_Z & 0 & \Delta E_X \\ \Omega & \Omega & -\Delta E_X & 0 & -\Delta E_Z & -\Delta E_X \\ 0 & 0 & 0 & \Delta E_X & -\Delta E_X & -E_Z \end{pmatrix} \tag{17}$$

if we constrain ourselves to the charge states (2,0), (0,2), and (1,1) with the associated spin states $\{|\uparrow\uparrow\rangle, |\uparrow\downarrow\rangle, |\downarrow\uparrow\rangle, |\downarrow\downarrow\rangle\}$. In addition, we define $\tilde{U} = U - U_{12}$, and for simplicity we set the y-component of the Zeeman term to zero.

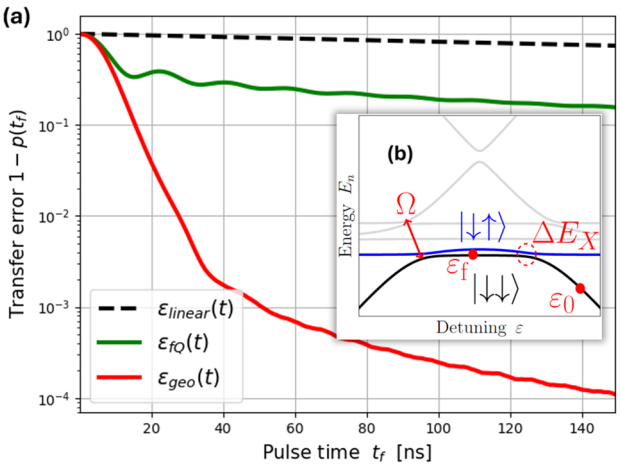

Figure 3 Adiabatic state initialization for truncated full DQD. **(a)** Transfer errors as a function of the pulse time t_f are plotted for the linear, standard fast-QUAD and geometric fast-QUAD protocols following Eq. (17) without incoherent errors. **(b)** Illustration of the 6x6 energy levels as a function of detuning, where we only focus on the two lower levels. The ST_- anti-crossing, which induces diabatic transitions in the initialization process, is given by the size of $\Delta E_X = 0.1$ GHz, similar to [87] for out-of-plane magnetic fields. After around 150 ns pulse time, we can expect a state transfer fidelity of 99.99% for the $|\downarrow\downarrow\rangle$ state by using the geometric fast-QUAD vastly outperforming the linear and standard fast-QUAD. Due to the sharpness of the standard fast-QUAD pulse, we find that it reduces the final state fidelity. The parameters used in the simulation are: $\tilde{U} = 100$ GHz, $E_Z = 10$ GHz, $\Omega = 10$ GHz, $\Delta E_Z = 1$ GHz, $\varepsilon_f = 10$ GHz, and $\varepsilon_0 = 3\tilde{U}/2$

Here, we restrict our optimization protocol to suppress only the transition of the ground state to the closest state. This way we effectively work in a low-energy two-dimensional subspace of the full 6x6 DQD, which in the eigenbasis takes the schematic form

$$\hat{H}_{\mathrm{DQD}} \approx \sum_{n,m=0,1} H_{n,m} \, |\psi_n\rangle\langle\psi_m| \, . \tag{18}$$

The state $|T_-\rangle = |\downarrow\downarrow\rangle$ is initialized by shifting the detuning $\varepsilon(t)$, which is the difference of the left and right chemical potentials of each dot $\varepsilon := V_L - V_R$. Due to the small ST_- anti-crossing, as found in [87] for out-of-plane magnetic fields, we again find that the geometric fast-QUAD is superior to the linear pulse and standard fast-QUAD (See Fig. 3). Even under this simplification, we report a transfer fidelity of > 99.99% after around 150 ns pulse time. However, one may also include more excited states to improve upon the geometric fast-QUAD in the adiabatic limit. In the Methods section, we analyze the behavior of the geometric fast-QUAD as one includes sequentially more excited states. Our findings show that in the adiabatic limit ($\delta \ll 1$) adding more energy eigenstates results in higher fidelities. For shorter times, the gain in state transfer fidelity is not guaranteed due to interference effects and non-adiabatic corrections.

1.3 Complete analysis of three-level model

To provide a more in-depth, yet simplified model that captures spin-to-charge conversion (See Fig. 4(a)), we restrict ourselves to a double dot system with a magnetic field pointing purely in the z-direction, neglecting the fully polarized states $|T_\pm\rangle$, and focus on the singlet-triplet basis with two charge degrees of freedom (Fig. 4(b)). The Hilbert space is

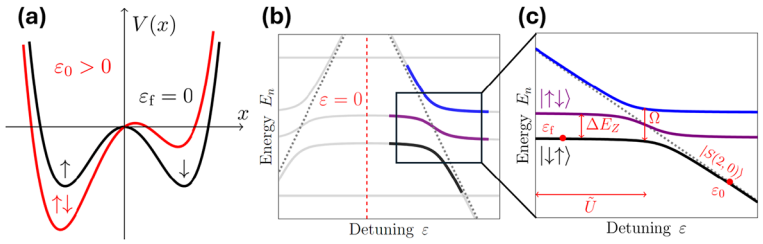

Figure 4 Adiabatic state initialization using PSB in spin qubit platforms. **(a)** Illustration of the spin-to-charge conversion protocol of spin qubits. The particle on the right side of the DQD potential can only be transferred to an antisymmetric spin state on the left side due to the Pauli exclusion principle. **(b)** Plot of the energy spectrum E_n of the full model (17) as a function of the detuning ε (tilt of the potential wells). The colored lines correspond to the energy levels of the reduced three-level model (22). **(c)** Detailed energy spectrum for the three-level Hamiltonian (22). The dashed line represents the energy of the $|S(2,0)\rangle$ state, which for large detuning $\varepsilon \gg \tilde{U}, \Omega, \Delta E_Z$ becomes the ground state of the DQD Hamiltonian

spanned by the following basis states

$$|S(2,0)\rangle = \hat{c}^\dagger_{L,\uparrow}\hat{c}^\dagger_{L,\downarrow}|\text{vac}\rangle \tag{19}$$

$$|S(1,1)\rangle = \frac{1}{\sqrt{2}}\left(\hat{c}^\dagger_{L,\uparrow}\hat{c}^\dagger_{R,\downarrow} - \hat{c}^\dagger_{L,\downarrow}\hat{c}^\dagger_{R,\uparrow}\right)|\text{vac}\rangle \tag{20}$$

$$|T_0(1,1)\rangle = \frac{1}{\sqrt{2}}\left(\hat{c}^\dagger_{L,\uparrow}\hat{c}^\dagger_{R,\downarrow} + \hat{c}^\dagger_{L,\downarrow}\hat{c}^\dagger_{R,\uparrow}\right)|\text{vac}\rangle\,, \tag{21}$$

where (n_L, n_R) describes the number of charges in the left and right dots, respectively, and $|\text{vac}\rangle$ represents the vacuum state. In this subspace, we find that the matrix representation of the DQD Hamiltonian, in the above basis, is

$$\hat{H}(t) = \begin{pmatrix} \tilde{U} - \varepsilon(t) & \Omega & 0 \\ \Omega & 0 & \Delta E_Z \\ 0 & \Delta E_Z & 0 \end{pmatrix}. \tag{22}$$

The energy spectrum of the Hamiltonian in Eq. (22) is seen in Fig. 4(c), which displays an anti-crossing at $\varepsilon = \tilde{U}$. The size of the anti-crossing is now determined by the combination of the tunnel coupling Ω and the Zeeman splitting difference ΔE_Z. In contrast to the Landau-Zener-Majorana-Stueckelberg anticrossing, the energy spectrum is not symmetric in the detuning ε. Also, the existence of a third energy level, makes it possible for diabatic transitions from the ground state to two upper energy eigenstates.

For concreteness and without loss of generality, we will focus in our analysis only on the initialization process, as the readout process is directly provided by the reverse pulse shape. The initial state is the singlet state in the (2,0) charge state and is adiabatically pulsed to the desired final state. Under coherent evolution, the only error source is due to undesired diabatic transitions, inducing interference effects that reduce the transfer fidelity. We scan multiple pairs of parameters and simulate the transfer error $1 - p(t_f)$ using the geometric fast-QUAD protocol in Eq. (7), the standard fast-QUAD and the linear protocol. For the geometric fast-QUAD protocol, we generate an appropriate adiabaticity using the boundary conditions of the detuning $(\varepsilon_0, \varepsilon_f)$ and the pulse time t_f with Eq. (6) and then feed the numerically solved pulse $\varepsilon_{\text{num}}(t)$ into our Hamiltonian or Lindbladian based time

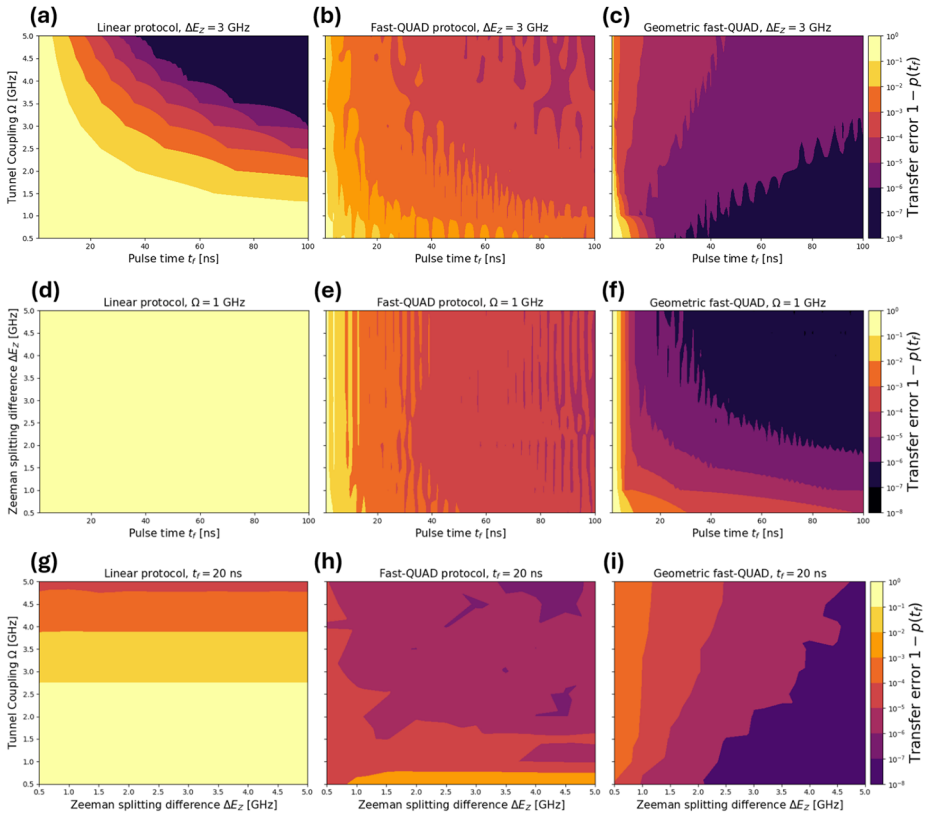

Figure 5 Comparison of initialization pulses using the linear *(a, d, g)*, standard fast-QUAD *(b, e, h)* and geometric fast-QUAD *(c, f, i)* protocols. Boundary conditions are $\varepsilon_0 = 2\tilde{U} = 200$ GHz and $\varepsilon_f = 0$. Figures **a-c** illustrate the effect of both the tunnel coupling and the pulse time on the transfer error. We note that the geometric fast-QUAD achieves a transfer fidelity of 99.99% after 20 ns, which defines a lower bound. Transfer errors as low as 10^{-8} may be reached even for small tunnel couplings. Figures **d-f** are contour plots sweeping the Zeeman splitting difference and the pulse time $(\Delta E_Z, t_f)$ at fixed tunnel coupling $\Omega = 1$ GHz. Here, the clear advantage of the geometric fast-QUAD comes through, as the size of the anti-crossing hinders the coherent charge transfer in the linear case and in the case of standard fast-QUAD, provides issues in the pulse timing and calibration. Hence, the standard fast-QUAD achieves lower final state fidelities. A similar trend can be seen in **g-i**. Remarkably, in **(h, i)** the charge transfer fidelity for both the standard and geometric fast-QUAD are lower bounded at 99%, independent of the combination $(\Delta E_Z, \Omega)$ for an ultrafast pulse with pulse time $t_f = 20$ ns. The geometric fast-QUAD provides lower achievable fidelities compared to the standard fast-QUAD. Note that, due to the conservation of energy along adiabatic paths, we observe no difference between the initialization and readout protocols

evolution, depending on whether we want to study unitary or non-unitary dynamics. Figure 5 shows the results of the geometric fast-QUAD pulse for the initialization sequence of the $|\downarrow\uparrow\rangle$ state of the Hamiltonian (22). The transfer error is reduced as a function of the pulse time as we move more adiabatic at larger pulse times. We observe the advantage of using the geometric fast-QUAD over the standard fast-QUAD and linear protocols as a reliable protocol for circumventing coherent errors, even for very small anti-crossings and extremely fast pulse times without the need to perfectly time the pulse. Strikingly, we observe as a common trend, that the transfer fidelity for the (geometric) fast-QUAD for $t_f > 20$ ns yields a transfer fidelity $\mathcal{F} > 99\%$ for all investigated settings of tunnel couplings Ω and Zeeman splitting differences ΔE_Z. Note that these results, for the same parameter settings besides the detuning boundary conditions, also hold for the adiabatic readout protocol, as the energy is conserved along these paths.

1.4 Incoherent dynamics due to quasistatic and Lindbladian noise

During coherent spin-to-charge conversion, a dominant error source are diabatic transitions in the vicinity of the anti-crossings, where the energy level difference is minimal. Our geometric protocol Eq. (4) is designed to minimize such errors. However, non-unitary dynamics arise due to couplings with ambient degrees of freedom, which alter the time evolution and hence may affect the optimal pulse shape. In the following, we will describe two ubiquitous noise types that may affect the protocol, low- and high-frequency charge noise.

One of the most known types of noise in semiconducting and superconducting devices is the appearance of low-frequency noise [68, 81, 98–103], whose noise spectral density follows $S(f) \propto 1/f$. Under sufficient conditions, the noise spectral density is the Fourier transform of the autocorrelation of the noise. For the Hamiltonian in Eq. (22), the noise spectral density arises from the correlation function of the fluctuations of the detuning parameter $\delta\varepsilon(t)$, which we include as a perturbation

$$\delta\hat{H}(t) = -\delta\varepsilon(t)\,|S(2,0)\rangle\langle S(2,0)| = -\delta\varepsilon(t)\,\hat{\Pi}_{\mathrm{S}(2,0)}, \tag{23}$$

where $\delta\varepsilon$ is drawn from a Gaussian distribution $\delta\varepsilon \sim \mathcal{N}(0,\sigma^2)$, which is centered at zero with a variance given by σ^2. In the simulations, we will model this behavior by fluctuating boundary conditions of the pulse shape $\varepsilon_{0,\mathrm{f}} \to \varepsilon_{0,\mathrm{f}} + \delta\varepsilon$ [104] and illustrate the differences between a noisy and a noiseless time evolution.

To study high-frequency noise, we will adopt the Lindblad master equation, which describes non-unitary evolution of a quantum system subject to Markovian noise. It takes the form

$$\frac{\mathrm{d}\hat{\rho}}{\mathrm{d}t} = -i\,[\hat{H},\hat{\rho}] + \sum_j \left(\hat{L}_j\hat{\rho}\hat{L}_j^\dagger - \frac{1}{2}\{\hat{L}_j^\dagger\hat{L}_j,\hat{\rho}\}\right), \tag{24}$$

where $\hat{L}_j$ are the conventional Lindblad operators. Explicitly, we describe dephasing from high-frequency noise via the dephasing jump operator [66]

$$\hat{L}_{\mathrm{dephasing}} = \sqrt{\frac{1}{2T_2}}\begin{pmatrix} 1 & 0 & 0 \\ 0 & -1 & 0 \\ 0 & 0 & -1 \end{pmatrix}. \tag{25}$$

Here the Lindblad operator acts on the charge states (1,1) and (2,0). The strength of the dephasing is captured by the decoherence time T_2. Since the dephasing operator has Hermitian real entries, we can also shift the Lindbladian to obtain the equivalent dephasing operator

$$\hat{L}'_{\mathrm{dephasing}} = \hat{L}_{\mathrm{dephasing}} + \sqrt{\frac{1}{2T_2}}\,\hat{\mathbb{1}} = \sqrt{\frac{2}{T_2}}\,\hat{\Pi}_{\mathrm{S}(2,0)}, \tag{26}$$

which will generate the same time dynamics. Since for spin qubits relaxation is several orders of magnitude longer than dephasing for spin [58] and charge qubits [105], we neglect it in our analysis. Note that relaxation usually benefits adiabatic charge transfer of the ground-state as it counteracts the diabatic transitions to energetically excited states,

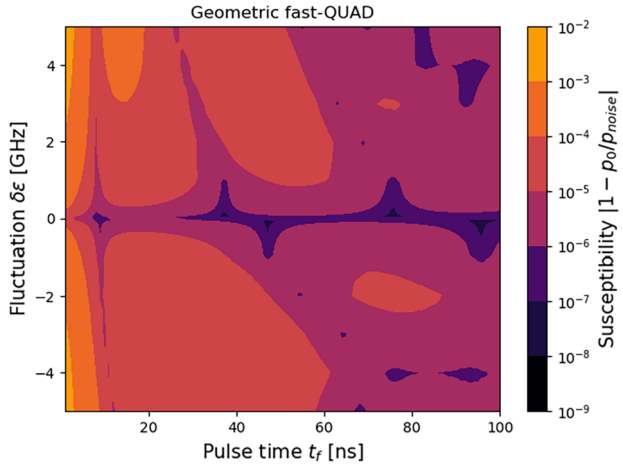

Figure 6 Susceptibility of the geometric fast-QUAD to low-frequency detuning fluctuations. We simulate the effects of quasistatic noise via a fluctuation in the detuning (23). This fluctuation will affect the initial and final boundary conditions when simulating the pulse shape as follows: $\varepsilon_{0,\mathrm{f}} \to \varepsilon_{0,\mathrm{f}} + \delta\varepsilon$. We fix the values of the tunnel coupling to $\Omega = 3$ GHz, $\Delta E_Z = 0.5$ GHz, and the remaining are identical to the ones in Fig. 5. The errors mostly affect infidelities below $1 - \mathcal{F} < 10^{-4}$ after a pulse time of $t_\mathrm{f} = 20$ ns. The asymmetry of the deviation is due to the fact that the energy spectrum is asymmetric around the anti-crossing at $\varepsilon = \tilde{U}$

thus effectively improving the population transfer fidelity. Using the Uhlmann fidelity $\mathcal{F}$ defined as

$$\mathcal{F}(\rho,\sigma) = \left(\mathrm{tr}\sqrt{\sqrt{\rho}\sigma\sqrt{\rho}}\right)^2, \tag{27}$$

we can determine the overlap of the lowest energy eigenstate $|\psi_0(t)\rangle$ and the time-evolved one under the non-unitary evolution given by (26) for the linear, standard fast-QUAD and geometric fast-QUAD state transfer protocols.

In addition to providing higher fidelities for very short pulse times and dense energy spectra, our protocol is also highly resilient against quasistatic noise as seen in Fig. 6, where we plotted the susceptibility of the transfer fidelity with respect to detuning fluctuations. Notably, after 20 ns the effects of the quasistatic noise affect the fidelities below 10^{-4}, even for strong fluctuation of $\delta\varepsilon = 5$ GHz. In Fig. 7 we also show that the geometric protocol is robust against pulse miscalibration regarding $\Omega \to \Omega + \delta\Omega$, for small $\delta\Omega$ and for pulse times bigger than 20 ns. Remarkably, assuming larger tunnel couplings for the pulse leads to smaller deviations from the calibrated result. This may be caused due to favorable interference effects in the initial ramp towards the anti-crossing. Namely, assuming a smaller anti-crossing will usually result in an initial fast ramping ending in a slow-down at the anti-crossing, leading to interference effects that do not destructively interfere beyond the anti-crossing.

Lastly, we compare the optimal control sequences of the linear, standard fast-QUAD, and geometric fast-QUAD protocol given some fixed decoherence time T_2 in Fig. 8. Here, we compute the linear, standard fast-QUAD, and geometric fast-QUAD pulse shapes and simulate the Uhlmann fidelity of the lowest energy eigenstate $|\psi_0(t_\mathrm{f})\rangle$ and the resulting mixed density matrix $\rho(t_\mathrm{f})$ under Lindbladian time evolution. For a fixed interval of allowed pulse operation times $t_\mathrm{f} \leq 50$ ns, we find the maximum Uhlmann fidelity at fixed decoherence time and compare the protocols. The maximum Uhlmann fidelity $\mathcal{F}(t_\mathrm{f}^*)$ is

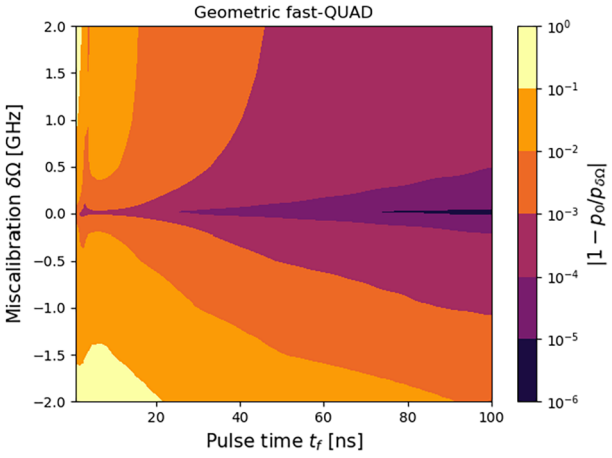

Figure 7 Transfer fidelity deviation, due to a miscalibrated pulse. The miscalibration is due to the tunnel coupling $\Omega_{\text{pulse}} = \Omega_0 + \delta\Omega$, where the system Hamiltonian is set at $\Omega_0 = 3$ GHz and $\Delta E_Z = 0.5$ GHz. Remarkably, assuming a bigger tunnel coupling for the pulse will deviate less from the calibrated result

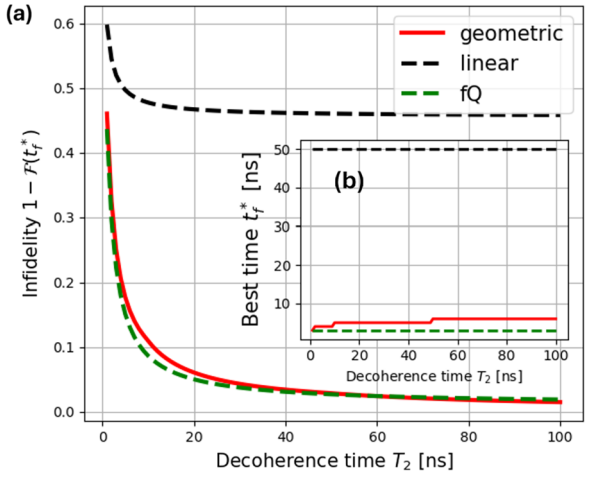

Figure 8 Fidelity analysis under non-unitary evolution. **(a)** Plot of the minimum infidelity of the standard fast-QUAD (green, dashed), geometric fast-QUAD (red line), and linear protocol (black, dashed line) for a fixed decoherence time T_2 for pulses up to 50 ns. The standard and geometric fast-QUAD protocols, even under dephasing noise and dense energy spectra ($\Omega = 1$ GHz, $\Delta E_Z = 1$ GHz), do always provide higher fidelity protocols at ultrafast operation times ($t_f^* < 10$ ns) than the linear one. The boundary conditions chosen are: $\varepsilon_0 = 2\tilde{U} = 200$ GHz, and $\varepsilon_f = 0$. **(b)** Best pulse operation times as a function of decoherence time T_2. Note that the linear protocol, due to the fact that it induces diabatic transitions, will always pick the longest operation time to achieve the highest fidelity

given by the optimal pulse operation time t_f^* for any given decoherence time T_2. The linear protocol will always perform best at the longest allowed pulse times to suppress the diabatic transitions which dominate in this regime. On the other hand, the (geometric) fast-QUAD will be optimal at ultrafast operation times ($t_f^* < 10$ ns) to simultaneously reduce the coherent and incoherent errors due to dephasing. Therefore, the (geometric) fast-QUAD will always outperform the linear protocol under fixed decoherence rates. In the limit of strong dephasing both the standard and geometric fast-QUAD perform similarly.

2 Discussion

In this work, we established a relationship between the quantum geometric structure of the Hilbert space and quasiadiabatic time dynamics. Our main focus lied in providing a general framework to deal with coherent errors arising from undesired diabatic transitions between multiple energy levels while operating at fast pulse times. Special emphasis was put on applying these methods to enable fast and high-fidelity adiabatic initialization and readout for a DQD system, which is integral for the minimization of state-dependent crosstalk. Nevertheless, we stress that the framework is applicable to all quantum systems with non-degenerate eigenvalues and only requires optimization on the level of the Hamiltonian and not the time-ordered evolution operator. For coherent evolution, we found that independent of the parameter configuration, the geometric fast-QUAD provides an upper bound on the transfer error at 10^{-2} for pulse times of 20 ns. Miscalibration of the pulse and quasistatic noise did not yield significant deviations and hence illustrate the robustness of the geometric fast-QUAD. For completion, errors arising due to strong dephasing effects were studied, and it was found that the (geometric) fast-QUAD is always superior to the linear protocol with respect to the Uhlmann fidelity, while allowing ultrafast operation times.

Nevertheless, further efforts in the understanding of the quantum geometric approach have to be made, especially with a focus on including the effects of noise directly into the formalism [106, 107], understanding the geometric difference between pure and mixed states, and what the impact of a non-abelian connection and degenerate eigenstates would be for transfer protocols. So far, the case of mixed states has been tackled only for full and finite rank density matrices [108, 109], making it challenging to capture non-unitary time evolution and systems with infinite-dimensional Hilbert spaces. The Choi-Jamiolkowski isomorphism allows a straightforward extension to unitary gates, giving rise to a formalism similar to the works in [12, 15]. An interesting avenue would also be to explore numerical optimization methods based on geometric cost functions, akin to using GRAPE, as shown in [110], for state-transfer protocols. In conclusion, the quantum geometry of parameter space will provide new opportunities for ultrafast adiabatic operations, allowing for significant improvements in the coherent processing of quantum information and accelerating the advancement of emerging quantum technologies.

3 Methods

3.1 Fundamentals of quantum Riemannian geometry

Bloch sphere from quantum geometry To define the metric g we need to find a basis $t_\mu(x)$ that spans the tangent space $T_{\hat{\rho}}P(\mathcal{H})$. A natural choice is given by the set of traceless and Hermitian matrices

$$t_\mu(x) = \partial_\mu \hat{\rho}(x) = \left|\partial_\mu \psi\right\rangle\!\left\langle\psi\right| + \left|\psi\right\rangle\!\left\langle\partial_\mu \psi\right|, \tag{28}$$

where we assume that the density matrices are pure $\hat{\rho}(x) = |\psi(x)\rangle\langle\psi(x)|$ and that the derivative is with respect to the parameters x^μ. We can define the quantum geometric tensor as the Killing form on the tangent space $T_{\hat{\rho}}P(\mathcal{H})$

$$g_{\mu\nu} = \frac{1}{2}\,\mathrm{tr}\left(t_\mu t_\nu\right) \tag{29}$$

$$= \mathrm{Re}\left[\langle \partial_\mu \psi | \partial_\nu \psi \rangle\right] + \langle \partial_\mu \psi | \psi \rangle \langle \psi | \partial_\nu \psi \rangle \,. \tag{30}$$

The above equation holds for any state vector in Hilbert space. If we restrict ourselves to energy eigenstates we can use the Hellmann-Feynman theorem to arrive at Eq. (2) in the main text. We note that the quantum geometric tensor (QGT) has certain symmetries, which, in part, will constrain our dynamics. First, the QGT is invariant under shifts in the ground state energy $\hat{H} \to \hat{H} + \omega(x)\hat{\mathbb{1}}$, which is the known invariance that only energy differences are measurable and is the expected invariance under a global $U(1)$ transformation. Secondly, the QGT does not change if we rescale the Hamiltonian globally with a function $\Omega(x)$, i.e. $\hat{H} \to \Omega(x)\hat{H}$, which we will refer to as conformal invariance. We also need to rescale the time variable to not affect the time dynamics. The conformal invariance will constrain our dynamics to a $(\dim \mathcal{M} - 1)$-dimensional subspace. To see this, we will work through the example in the main text: A general 2×2 Hamiltonian can be written in the Pauli basis, which in polar coordinates (ρ, ϕ, z) takes the form

$$\hat{H}_{\text{Pauli}} = \begin{pmatrix} z & \rho\, e^{-i\phi} \\ \rho\, e^{i\phi} & -z \end{pmatrix}, \tag{31}$$

where we note that, for pure states, $\dim P(\mathcal{H}_{\text{Pauli}}) = 2 < \dim \mathcal{M} = 3$, as pure states can be fully described by the angles (θ, ϕ) on the Bloch sphere. This condition restricts the notion of $\mathcal{M}$ being an embedding of the projective Hilbert space $P(\mathcal{H}_{\text{Pauli}})$ as the map is no longer injective. Due to the conformal invariance, however, we may restrict ourselves to subspaces that span the projective Hilbert space and hence form a well-defined embedding. For instance, if we identify $x^\mu = \{\rho, \phi, z\}$ then we may find a function $\Omega(x)$ such that we can reduce the number of parameters. If we want to work in the subspace of $x^\mu = \{\rho, z\}$ we find that the quantum metric tensor is singular, i.e. $\det g = 0$, which alludes to the fact that the embedding is ill-defined. This feature can be seen by the fact that there is no non-trivial function $\Omega(x)$ that removes the ϕ-dependence. On the other hand, the subsets $x^\mu = \{\rho, \phi\}$ and $x^\mu = \{\phi, z\}$ can be well-defined. For instance, if $\Omega(x) = z$ and we redefine $\rho/z \to \rho$, the Pauli Hamiltonian takes the form

$$\hat{H}_{\text{Pauli}} = \begin{pmatrix} 1 & \rho\, e^{-i\phi} \\ \rho\, e^{i\phi} & -1 \end{pmatrix}, \tag{32}$$

which, upon using Eq. (2), leads to a non-singular quantum metric tensor

$$[g_{\mu\nu}(\rho, \phi)] = \frac{1}{4(1+\rho^2)} \begin{pmatrix} \frac{1}{(1+\rho^2)} & 0 \\ 0 & \rho^2 \end{pmatrix}, \tag{33}$$

which captures the fact that the embedding is well-defined. This can also be seen by the fact that now $\dim P(\mathcal{H}_{\text{Pauli}}) = \dim \mathcal{M}$. This metric is the metric on the Bloch sphere, as can be seen if we use $\rho = \tan\theta$ and use the transformation rule for the quantum metric tensor to arrive at

$$[g_{\mu\nu}(\theta, \phi)] = \frac{1}{4} \begin{pmatrix} 1 & 0 \\ 0 & \sin^2\theta \end{pmatrix}. \tag{34}$$

Finally, we want to note that the quantum metric tensor, due to the definition as a formal distance metric on the space of state vectors, only depends on the topology of the manifold and is, hence, a frame-independent object different from the works in [74, 75, 111]. For instance, the topology of the single-qubit system is $P(\mathcal{H}_{\text{Pauli}}) = \mathbb{CP}^1$, which is the complex projective space or Riemann sphere.

Beltrami identity, Killing charges and energy fluctuations To derive that adiabatic geometric condition (4) we start by simplifying the length functional in the main text via the Cauchy-Schwarz relation to the following functional [78]

$$\mathcal{L}'[x,\dot{x}] = \int_0^{t_f} dt \left[g_{\mu\nu}(x)\dot{x}^\mu \dot{x}^\nu \right], \tag{35}$$

where the integrand can be understood as a Lagrangian $L[x,\dot{x},t]$ and the functional as the action. If the Lagrangian does not explicitly depend on time, i.e. $\partial L/\partial t = 0$, then Beltrami's identity holds

$$\dot{x}^\alpha \frac{\partial L}{\partial \dot{x}^\alpha} - L = \text{const.} \tag{36}$$

The left-hand side is the expression of the Hamiltonian, and hence, in this case, Beltrami's identity is a consequence of conservation of energy. Computing the partial derivative of the Lagrangian above using $\partial \dot{x}^\mu / \partial \dot{x}^\alpha = \delta^\mu_\alpha$ we find the adiabatic-geometric condition

$$g_{\mu\nu}(x)\dot{x}^\mu \dot{x}^\nu = \text{const.} \tag{37}$$

Another way to see this identity is that conservation laws arise due to symmetries. The connection between symmetry and conserved quantities in the geometrical context is illustrated by the Killing vectors ξ^μ. Each Killing vector has an associated conserved charge [49]

$$\partial_t Q_\xi = \partial_t \left(g_{\mu\nu}(x)\xi^\mu \dot{x}^\nu \right) = 0. \tag{38}$$

If the Killing vector is proportional to the tangent vector $\xi^\mu \propto \dot{x}^\mu$ we also find the adiabatic-geometric relation. This shows the explicit relation between energy conservation and geometry. In order to find the geodesics of a manifold one also only needs $\dim \mathcal{M} - 1$ Killing vector fields [49], which aligns with the parameter subspace after the constraint due to the conformal invariance of the QGT.

3.2 Constraints in the geometric fast-QUAD

The geometric fast-QUAD protocol can be understood as extremizing the length functional $\mathcal{L}[x,\dot{x};t]$ and, hence, providing a minimum that is robust against parameter fluctuations. The framework is also flexible enough to include constraints that may be imposed on the physical system. This can be done via the inclusion of a Lagrange multiplier λ and an associated constraint functional $\mathcal{C}[x,\dot{x}]$, yielding a new length functional

$$\tilde{\mathcal{L}}[x,\dot{x}] = \mathcal{L}[x,\dot{x}] + \lambda\, \mathcal{C}[x,\dot{x}]. \tag{39}$$

The geodesic equations, which constitute the minimum of the length functional $\delta\mathcal{L} = 0$, are now altered to

$$0 = \delta\tilde{\mathcal{L}}[x, \dot{x}] \tag{40}$$

$$= \delta\mathcal{L}[x, \dot{x}] + \lambda\, \delta\mathcal{C}[x, \dot{x}], \tag{41}$$

which yield new sets of differential equations that explicitly depend on the constraint $\mathcal{C}$, similar to the case of the quantum brachistochrone [14, 16]. Note that including a general constraint $\mathcal{C}$ may break the symmetries of the original length functional $\mathcal{L}$, resulting in the breaking of our geometric fast-QUAD protocol (4).

3.3 Optimality of geometric-adiabatic protocol

Here we will show that our quantum geometric approach is equivalent to minimizing the energy fluctuations. Starting from the second-order Taylor expansion of the wave function

$$|\psi(t + dt)\rangle \approx |\psi(t)\rangle + \frac{\mathrm{d}}{\mathrm{d}t}|\psi(t)\rangle\, dt + \frac{1}{2}\frac{\mathrm{d}^2}{\mathrm{d}t^2}|\psi(t)\rangle\, dt^2, \tag{42}$$

and using the Schroedinger equation, we also find

$$|\psi(t + dt)\rangle \approx |\psi(t)\rangle + \Big(-iH\Big)|\psi(t)\rangle\, dt + \frac{1}{2}\left(-i\frac{\mathrm{d}H}{\mathrm{d}t} - H^2\right)|\psi(t)\rangle\, dt^2. \tag{43}$$

Similar to the main text, we compare this infinitesimally evolved state with the initial state to compute the fidelity (up to second-order terms)

$$|\langle\psi(t)|\psi(t + dt)\rangle|^2 \approx 1 - \Big(\langle H^2\rangle - \langle H\rangle^2\Big)dt^2 \tag{44}$$

$$\approx 1 - \sigma_E^2 dt^2. \tag{45}$$

This means that in order to stay adiabatic, one needs to minimize the energy fluctuations σ_E^2. This fidelity is exactly mapped out by the quantum metric tensor, as seen in the main text

$$1 - |\langle\psi(t)|\psi(t + dt)\rangle|^2 \approx \sigma_E^2 dt^2 \tag{46}$$

$$1 - |\langle\psi(x)|\psi(x + dx)\rangle|^2 \approx \frac{1}{2}g_{\mu\nu}(x)dx^\mu dx^\nu, \tag{47}$$

hence we find that the quantum geometric protocol achieves the optimal adiabatic protocol (up to second order)

$$\min\left(g_{\mu\nu}(x)\frac{\mathrm{d}x^\mu}{\mathrm{d}t}\frac{\mathrm{d}x^\nu}{\mathrm{d}t}\right) = \min\Big(2\,\sigma_E^2\Big). \tag{48}$$

3.4 Numerical methods

Here we outline the numerical methods used in the main text, including the generation of the pulse shapes, the Hamiltonian, and the Lindblad master equation solvers.

Pulse shape interpolation First, we compute the quantum metric tensor using Eq. (29). Making use of the quantum adiabatic condition (4), we obtain a differential equation for the pulse in terms of the adiabaticity parameter δ. In the single-parameter case, where we focus on the detuning $\varepsilon(t)$ as our control parameter, we find

$$\left(\frac{\mathrm{d}\varepsilon}{\mathrm{d}t}\right)^2 = \delta^2 \left[\sum_{n\neq 0} \frac{|\langle\psi_0|\partial_\varepsilon \hat{H}|\psi_n\rangle|^2}{(E_n - E_0)^2}\right]^{-1}, \tag{49}$$

for the geometric fast-QUAD method, and

$$\left(\frac{\mathrm{d}\varepsilon}{\mathrm{d}t}\right)^2 = \delta^2 \left[\sum_{n\neq 0} \frac{|\langle\psi_0|\partial_\varepsilon \hat{H}|\psi_n\rangle|^2}{(E_n - E_0)^4}\right]^{-1}, \tag{50}$$

for the standard fast-QUAD. As mentioned in the main text, the cost function in our framework corresponds to the quantum metric tensor $g_{\varepsilon\varepsilon}$, whereas the standard fast-QUAD differs by the factor of 2 in the energy splitting, thereby missing the geometric interpretation. With appropriate boundary conditions, we can compute the adiabaticity parameter using Eq. (6) as follows

$$\delta = \frac{1}{t_\mathrm{f}} \int_{\varepsilon(0)}^{\varepsilon(t_\mathrm{f})} d\varepsilon \sqrt{\sum_{n\neq 0} \frac{|\langle\psi_0|\partial_\varepsilon \hat{H}|\psi_n\rangle|^2}{(E_n - E_0)^2}}, \tag{51}$$

and similarly for the standard fast-QUAD. Finally, we solve the above differential equation for the pulse numerically (See Fig. 9).

Computational complexity We note that the computational complexity of generating the pulses is mainly determined by the diagonalization bottleneck. For a $N \times N$ dense Hamiltonian matrix, one requires $\mathcal{O}(N^3)$ operations to fully diagonalize the system. However, in our framework, we can naturally restrict ourselves to the closest k eigenvalues and eigenvectors, therefore achieving a reduced time complexity of $\mathcal{O}(N^2 k)$.

In contrast, for instance, numerical methods like GRAPE typically require a computational complexity of $\mathcal{O}(KLN^3)$ [110], where K is the total number of control parameters and L is the number of iteration steps. However, we note that approximate Krylov methods can reduce the time-complexity of GRAPE to $\mathcal{O}(KLN^2 k)$, where k is the dimension of the Krylov subspace, at the cost of restrictions on the time intervals [112]. We also note that the required iteration steps of GRAPE can be strongly decreased using a geometric gate optimization [110]. Faster convergence is achieved using geometric updates, as opposed to the GRAPE updates, that follow the geodesic path to the target gate, at the cost of a steeper $\mathcal{O}(N^4)$ dependence.

Hamiltonian simulation For the numerical simulations of the coherent population transfer, we first generate a pulse according to the boundary conditions for initialization or readout. Next, we replace the numerically solved pulse $\varepsilon_\mathrm{num}(t)$ in the Hamiltonian operator and then solve the Schrödinger equation (in units of $\hbar = 1$)

$$i\frac{\mathrm{d}}{\mathrm{d}t}|\psi(t)\rangle = \hat{H}[\varepsilon_\mathrm{num}(t)]\,|\psi(t)\rangle\,. \tag{52}$$

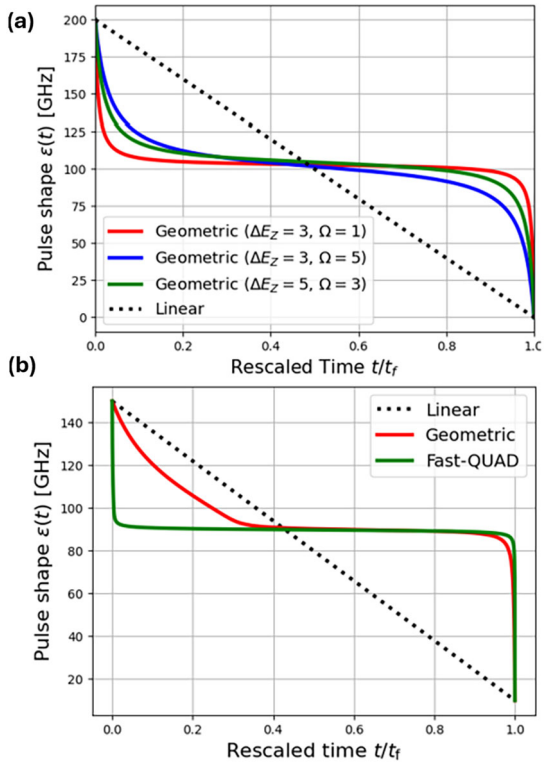

Figure 9 Control pulse shapes for the initialization protocol. (a) Given the Hamiltonian in Eq. (22), we numerically solve for the pulse shape $\varepsilon_{\text{num}}(t)$ using the geometric fast-QUAD (4). (b) Detuning pulse shapes for the analysis of the truncated full DQD shown in Fig. 3. However, here we illustrate the differences between the three main methods studied in this work: the linear, fast-QUAD, and geometric approaches

Given the initial state $|\psi_0(t=0)\rangle$, we evolve the state and project it onto the lowest energy eigenstate at the final pulse time to see whether coherent errors occurred. For that, we compute the transfer probability $p(t_{\text{f}}) = |\langle\psi_0(t_{\text{f}})|\psi_{\text{geo}}(t_{\text{f}})\rangle|^2$, where

$$|\psi_{\text{geo}}(t_{\text{f}})\rangle = \mathcal{T}\exp\left(-i\int_0^{t_{\text{f}}}\hat{H}[\varepsilon_{\text{num}}(t)]\right)|\psi_0(t=0)\rangle\,. \tag{53}$$

Lindblad simulation For the numerical simulations of the Lindblad master equation, we switch to the vectorized form. We choose to use vectorization by row, which means that, for instance,

$$\rho = \begin{pmatrix} a & b \\ c & d \end{pmatrix} \rightarrow |\rho\rangle\rangle = \text{vec}[\rho] = \begin{pmatrix} a \\ b \\ c \\ d \end{pmatrix} \tag{54}$$

In this notation, the Lindblad master equation can be written as a linear equation

$$\frac{\text{d}}{\text{d}t}|\rho\rangle\rangle = \hat{\mathcal{L}}\cdot|\rho\rangle\rangle, \tag{55}$$

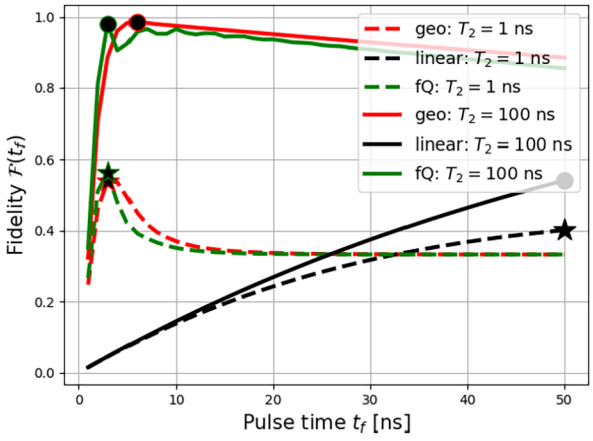

Figure 10 Example of simulated Uhlmann fidelity between the lowest energy eigenstate and the mixed state after Lindbladian evolution. The full (dashed) lines represent the fidelities for a dephasing time $T_2 = 100$ ns ($T_2 = 1$ ns) with the dots and the stars illustrating the maximum values of the overlap for the respective decoherence times

where the Lindbladian takes the form

$$\hat{\mathcal{L}} = -i\left(\hat{H} \otimes \hat{\mathbb{1}} - \hat{\mathbb{1}} \otimes \hat{H}^T\right) + \sum_j \hat{L}_j \otimes \hat{L}_j^* - \frac{1}{2}\left(\hat{L}_j^\dagger \hat{L}_j \otimes \hat{\mathbb{1}} + \hat{\mathbb{1}} \otimes [\hat{L}_j^\dagger \hat{L}_j]^T\right). \tag{56}$$

Note that the expression explicitly depends on the basis chosen, as the transpose is basis-dependent. To compute the success of the state transfer protocols we define the Uhlmann fidelity

$$\mathcal{F}(\rho, \sigma) = \left(\mathrm{tr}\sqrt{\sqrt{\rho}\sigma\sqrt{\rho}}\right)^2. \tag{57}$$

We will use this to quantify the overlap between the time-evolved pure initial state $|\psi_0(0)\rangle \approx |S(2,0)\rangle$ to the mixed state at the end of the non-unitary evolution $\rho(t_\mathrm{f})$. In this case, the fidelity simplifies to

$$\mathcal{F}(\rho(t_\mathrm{f}), |\psi_0(t_\mathrm{f})\rangle\langle\psi_0(t_\mathrm{f})|) = |\,\langle\psi_0(t_\mathrm{f})|\rho(t_\mathrm{f})|\psi_0(t_\mathrm{f})\rangle\,|. \tag{58}$$

Defining $|\psi_0\rangle\rangle = \mathrm{vec}[|\psi_0(t_\mathrm{f})\rangle\langle\psi_0(t_\mathrm{f})|]$ we find that the Uhlmann fidelity reduces to

$$\mathcal{F}(t_\mathrm{f}) = |\langle\langle\rho(t_\mathrm{f})|\psi_0(t_\mathrm{f})\rangle\rangle|. \tag{59}$$

Figure 10 shows the procedure to obtain the optimal control simulation in Fig. 8. We start by simulating the Uhlmann fidelity for a fixed decoherence time T_2 for pulse times $t_\mathrm{f} \in [0, 50]$ ns and extract the highest overlap for both the linear (dashed line) and geometric (full line) protocol. These are shown in the figure as blue circles/red stars for two exemplary decoherence times $T_2 = 1, 100$ ns, respectively. Note that the geometric protocol provides a higher fidelity at shorter pulse times. From each simulation, therefore, we extract the fidelity $\mathcal{F}(t_\mathrm{f}^*)$, the pulse time t_f^* at which the highest fidelity is reached, and the corresponding decoherence time T_2.

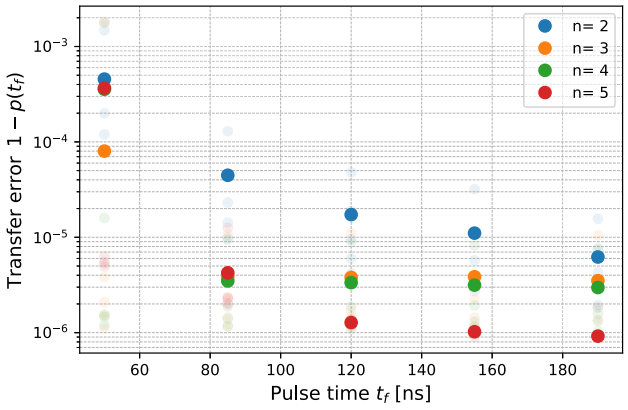

Figure 11 Coherent transfer errors for the model in Eq. (17) disregarding the very-high-energy state $|S(0,2)\rangle$. The main anti-crossing is the one governed by ΔE_X, hence, to avoid special resonance sweep spots we simulate the fidelity for $\Delta E_X = .1$ GHz to $\Delta E_X = 1$ GHz. We plot the average over these in bold. The number of excited states, labeled by n, improves the fidelity in the adiabatic limit. The parameters used in the simulation are: $\tilde{U} = 100$ GHz, $E_Z = 10$ GHz, $\Omega = 10$ GHz, $\Delta E_Z = 1$ GHz, $\varepsilon_f = 10$ GHz, and $\varepsilon_0 = 3\tilde{U}/2$

3.5 Full Hilbert space analysis

In the main text, we provide a framework flexible to be used for any quantum system. In Fig. 3, we provided the example of generating a geometric fast-QUAD pulse while only using 1 excited state. However, if we include more excited states, we find that, in the adiabatic limit, the pulse shape will yield higher fidelities. Here, we study the sequential inclusion of these excited states as shown in Fig. 11 and neglecting the state $|S(0,2)\rangle$, which is far-separated in energy $\approx 2\tilde{U}$. In bold, we plot the average for different ΔE_X to avoid specific resonances. Our results clearly show that additional energy eigenstates increase the fidelity as expected. However, we note that the gain in infidelity comes in steps and slows down for farther separated states, allowing for an efficient computation by truncation.

Acknowledgements
We thank the members of the Bosco, Rimbach-Russ, Veldhorst, Scappucci, and Vandersypen groups for helpful discussions on practical applications. Additionally, we are grateful for discussions with Amanda Seedhouse, David Fernández Fernández, and Edmondo Valvo about the theoretical model. This research was partly supported by the EU through the H2024 QLSI2 project and partly sponsored by the Army Research Office under Award Number: W911NF-23-1-0110. The views and conclusions contained in this document are those of the authors and should not be interpreted as representing the official policies, either expressed or implied, of the Army Research Office or the U.S. Government. The U.S. Government is authorized to reproduce and distribute reprints for Government purposes notwithstanding any copyright notation herein.

Author contributions
M.R.-R. conceived and supervised the project. C.V.M. developed the theoretical model, performed the simulations, and performed the analysis with input from S.B. and M.R.-R.. C.V.M. wrote the manuscript with input from S.B., and M.R.-R.

Data Availability
Simulation software and data analysis scripts supporting this work are available at https://doi.org/10.5281/zenodo.13871529.

Declarations

Competing interests
The authors declare no competing interests.

Received: 16 June 2025 Accepted: 30 September 2025 Published online: 31 October 2025

References

1. Glaser SJ, Boscain U, Calarco T, Koch CP, Köckenberger W, Kosloff R, Kuprov I, Luy B, Schirmer S, Schulte-Herbrüggen T, Sugny D, Wilhelm FK. Training Schrödinger's cat: quantum optimal control. Eur Phys J D. 2015;69:279.
2. Werschnik J, Gross EKU. Optimal optimal control theory. J Phys B, At Mol Opt Phys. 2007;40:18.
3. Poggiali F, Cappellaro P, Fabbri N. Optimal control for one-qubit quantum sensing. Phys Rev X. 2018;8:021059.
4. Theis LS, Motzoi F, Machnes S, Wilhelm FK. Counteracting systems of diabaticities using DRAG controls: the status after 10 years. Europhys Lett. 2018;123:60001.
5. James MR. Optimal quantum control theory. 2021.
6. Koch CP, Boscain U, Calarco T, Dirr G, Filipp S, Glaser SJ, Kosloff R, Montangero S, Schulte-Herbrüggen T, Sugny D, Wilhelm FK. Quantum optimal control in quantum technologies. Strategic report on current status, visions and goals for research in Europe. EPJ Quantum Technol. 2022;9:19.
7. Lidar DA, Brun TA, editors. Quantum error correction. Cambridge: Cambridge University Press; 2013.
8. Khaneja N, Brockett R, Glaser SJ. Time optimal control in spin systems. Phys Rev A. 2001;63:032308.
9. Carlini A, Hosoya A, Koike T, Okudaira Y. Time-optimal quantum evolution. Phys Rev Lett. 2006;96:060503.
10. Pontryagin LS. Mathematical theory of optimal processes. London: Routledge; 2017.
11. Boltyanski V, Martini H, Soltan V. Geometric methods and optimization problems. In: Du D-Z, Pardalos PM, editors. Combinatorial optimization. vol. 4. Boston: Springer; 1999.
12. Carlini A, Hosoya A, Koike T, Okudaira Y. Time-optimal unitary operations. Phys Rev A. 2007;75:042308.
13. Boscain U, Sigalotti M, Sugny D. Introduction to the Pontryagin maximum principle for quantum optimal control. PRX Quantum. 2021;2:030203.
14. Koike T. Quantum brachistochrone. Philos Trans R Soc A, Math Phys Eng Sci. 2022;380:20210273.
15. Rezakhani AT, Kuo W-J, Hamma A, Lidar DA, Zanardi P. Quantum adiabatic brachistochrone. Phys Rev Lett. 2009;103:080502.
16. Chernova KS, Stepanenko AA, Gorlach MA. Optimizing state transfer in a three-qubit array via quantum brachistochrone method. Opt Mater Express. 2025;15:578.
17. Zhuang F, Zeng J, Economou SE, Barnes E. Noise-resistant Landau-Zener sweeps from geometrical curves. Quantum. 2022;6:639.
18. Walelign HY. Dynamically corrected gates in silicon singlet-triplet spin qubits. Phys Rev Appl 2024;22. https://doi.org/10.1103/PhysRevApplied.22.064029.
19. Barnes E, Calderon-Vargas FA, Dong W, Li B, Zeng J, Zhuang F. Dynamically corrected gates from geometric space curves. Quantum Sci Technol. 2022;7:023001.
20. Buterakos D. Geometrical Formalism for Dynamically Corrected Gates in Multiqubit Systems. PRX Quantum. 2021;2. https://doi.org/10.1103/PRXQuantum.2.010341.
21. Khaneja N, Reiss T, Kehlet C, Schulte-Herbrüggen T, Glaser SJ. Optimal control of coupled spin dynamics: design of NMR pulse sequences by gradient ascent algorithms. J Magn Reson. 2005;172:296.
22. Goodwin DL, Vinding MS. Accelerated Newton-Raphson GRAPE methods for optimal control. Phys Rev Res. 2023;5:L012042.
23. Caneva T, Calarco T, Montangero S. Chopped random-basis quantum optimization. Phys Rev A. 2011;84:022326.
24. Rach N, Müller MM, Calarco T, Montangero S. Dressing the chopped-random-basis optimization: a bandwidth-limited access to the trap-free landscape. Phys Rev A. 2015;92:062343.
25. Bergmann K, Theuer H, Shore BW. Coherent population transfer among quantum states of atoms and molecules. Rev Mod Phys. 1998;70:1003.
26. Motzoi F, Gambetta JM, Rebentrost P, Wilhelm FK. Simple pulses for elimination of leakage in weakly nonlinear qubits. Phys Rev Lett. 2009;103:110501.
27. Berry MV. Transitionless quantum driving. J Phys A, Math Theor. 2009;42:365303.
28. De Grandi C, Polkovnikov A. Adiabatic perturbation theory: from Landau-Zener problem to quenching through a quantum critical point. Berlin: Springer; 2010. p. 75–114.
29. Vutha AC. A simple approach to the Landau-Zener formula. Eur J Phys. 2010;31:389.
30. Motzoi F, Gambetta JM, Merkel ST, Wilhelm FK. Optimal control methods for rapidly time-varying Hamiltonians. Phys Rev A. 2011;84:022307.
31. Chen X, Torrontegui E, Muga JG. Lewis-Riesenfeld invariants and transitionless quantum driving. Phys Rev A. 2011;83:062116.
32. Ribeiro H, Baksic A, Clerk AA. Systematic magnus-based approach for suppressing leakage and nonadiabatic errors in quantum dynamics. Phys Rev X. 2017;7:011021.
33. Sels D, Polkovnikov A. Minimizing irreversible losses in quantum systems by local counterdiabatic driving. Proc Natl Acad Sci USA. 2017;114:E3909.
34. Ban Y, Chen X, Platero G. Fast long-range charge transfer in quantum dot arrays. Nanotechnology. 2018;29:505201.
35. Takahashi K. Hamiltonian engineering for adiabatic quantum computation: lessons from shortcuts to adiabaticity. J Phys Soc Jpn. 2019;88:061002.
36. Ban Y, Chen X, Kohler S, Platero G. Spin entangled state transfer in quantum dot arrays: coherent adiabatic and speed-up protocols. Adv Quantum Technol. 2019;2:1900048.
37. Guéry-Odelin D, Ruschhaupt A, Kiely A, Torrontegui E, Martínez-Garaot S, Muga JG. Shortcuts to adiabaticity: concepts, methods, and applications. Rev Mod Phys. 2019;91:045001.
38. Setiawan F, Groszkowski P, Ribeiro H, Clerk AA. Analytic design of accelerated adiabatic gates in realistic qubits: general theory and applications to superconducting circuits. PRX Quantum. 2021;2:030306.
39. Takahashi K. Dynamical invariant formalism of shortcuts to adiabaticity. Philos Trans R Soc A, Math Phys Eng Sci. 2022;380:20220301.
40. Fernández-Fernández D, Ban Y, Platero G. Quantum control of hole spin qubits in double quantum dots. Phys Rev Appl. 2022;18:054090.
41. Glasbrenner EP, Schleich WP. The Landau–Zener formula made simple. J Phys B, At Mol Opt Phys. 2023;56:104001.
42. Rimbach-Russ M, Philips SGJ, Xue X, Vandersypen LMK. Simple framework for systematic high-fidelity gate operations. Quantum Sci Technol. 2023;8:045025.

43. Romero SV, Chen X, Platero G, Ban Y. Optimizing edge-state transfer in a Su-Schrieffer-Heeger chain via hybrid analog-digital strategies. Phys Rev Appl. 2024;21:034033.
44. Martínez-Garaot S, Ruschhaupt A, Gillet J, Busch Th, Muga JG. Fast quasiadiabatic dynamics. Phys Rev A. 2015;92:043406.
45. Xu J, Du Y-X, Huang W. Improving coherent population transfer via a stricter adiabatic condition. Phys Rev A. 2019;100:023848.
46. Fehse F, David M, Pioro-Ladrière M, Coish WA. Generalized fast quasiadiabatic population transfer for improved qubit readout, shuttling, and noise mitigation. Phys Rev B. 2023;107:245303.
47. Lambert J, Sørensen ES. From classical to quantum information geometry: a guide for physicists. New J Phys. 2023;25:081201.
48. Kolodrubetz M, Sels D, Mehta P, Polkovnikov A. Geometry and non-adiabatic response in quantum and classical systems. Phys Rep. 2017;697:1.
49. Liska D, Gritsev V. Hidden symmetries, the Bianchi classification and geodesics of the quantum geometric ground-state manifolds. SciPost Phys. 2021;10:020.
50. Juárez SB, Gonzalez D, Gutiérrez-Ruiz D, Vergara JD. Generalized quantum geometric tensor for excited states using the path integral approach. Phys Scr. 2023;98:095106.
51. Kolodrubetz M, Gritsev V, Polkovnikov A. Classifying and measuring geometry of a quantum ground state manifold. Phys Rev B. 2013;88:064304.
52. Ma Y-Q, Chen S, Fan H, Liu W-M. Abelian and non-Abelian quantum geometric tensor. Phys Rev B. 2010;81:245129.
53. Kobayashi T, Noiri A, Nakajima T, Takeda K, Camenzind LC, Jin IK, Scappucci G, Tarucha S. Charge-induced energy shift of a single-spin qubit under a magnetic-field gradient. 2024. arXiv:2411.16224.
54. Larrouy A, Patsch S, Richaud R, Raimond J-M, Brune M, Koch CP, Gleyzes S. Fast navigation in a large Hilbert space using quantum optimal control. Phys Rev X. 2020;10:021058.
55. Larocca M, Calzetta E, Wisniacki DA. Exploiting landscape geometry to enhance quantum optimal control. Phys Rev A. 2020;101:023410.
56. Scappucci G, Kloeffel C, Zwanenburg FA, Loss D, Myronov M, Zhang J-J, De Franceschi S, Katsaros G, Veldhorst M. The germanium quantum information route. Nat Rev, Mater. 2021;6:926.
57. Burkard G, Ladd TD, Pan A, Nichol JM, Petta JR. Semiconductor spin qubits. Rev Mod Phys. 2023;95:025003.
58. Stano P, Loss D. Review of performance metrics of spin qubits in gated semiconducting nanostructures. Nat Rev Phys. 2022;4:672.
59. Undseth B, Pietx-Casas O, Raymenants E, Mehmandoost M, Madzik MT, Philips SGJ, de Snoo SL, Michalak DJ, Amitonov SV, Tryputen L, Wuetz BP, Fezzi V, Esposti DD, Sammak A, Scappucci G, Vandersypen LMK. Hotter is easier: unexpected temperature dependence of spin qubit frequencies. Phys Rev X. 2023;13:041015.
60. Huang JY, Su RY, Lim WH, Feng M, van Straaten B, Severin B, Gilbert W, Dumoulin Stuyck N, Tanttu T, Serrano S, Cifuentes JD, Hansen I, Seedhouse AE, Vahapoglu E, Leon RCC, Abrosimov NV, Pohl H-J, Thewalt MLW, Hudson FE, Escott CC, Ares N, Bartlett SD, Morello A, Saraiva A, Laucht A, Dzurak AS, Yang CH. High-fidelity spin qubit operation and algorithmic initialization above 1 K. Nature. 2024;627:772.
61. Lanza M, Smets Q, Huyghebaert C, Li L-J. Yield, variability, reliability, and stability of two-dimensional materials based solid-state electronic devices. Nat Commun. 2020;11:5689.
62. Zwerver AMJ, Krähenmann T, Watson TF, Lampert L, George HC, Pillarisetty R, Bojarski SA, Amin P, Amitonov SV, Boter JM, Caudillo R, Correas-Serrano D, Dehollain JP, Droulers G, Henry EM, Kotlyar R, Lodari M, Lüthi F, Michalak DJ, Mueller BK, Neyens S, Roberts J, Samkharadze N, Zheng G, Zietz OK, Scappucci G, Veldhorst M, Vandersypen LMK, Clarke JS. Qubits made by advanced semiconductor manufacturing. Nat Electron. 2022;5:184.
63. Cifuentes JD, Tanttu T, Gilbert W, Huang JY, Vahapoglu E, Leon RCC, Serrano S, Otter D, Dunmore D, Mai PY, Schlattner F, Feng M, Itoh K, Abrosimov N, Pohl H-J, Thewalt M, Laucht A, Yang CH, Escott CC, Lim WH, Hudson FE, Rahman R, Dzurak AS, Saraiva A. Bounds to electron spin qubit variability for scalable CMOS architectures. Nat Commun. 2024;15:4299.
64. Lai NS, Lim WH, Yang CH, Zwanenburg FA, Coish WA, Qassemi F, Morello A, Dzurak AS. Pauli spin blockade in a highly tunable silicon double quantum dot. Sci Rep. 2011;1:110.
65. Niegemann DJ, El-Homsy V, Jadot B, Nurizzo M, Cardoso-Paz B, Chanrion E, Dartiailh M, Klemt B, Thiney V, Bäuerle C, Mortemousque P-A, Bertrand B, Niebojewski H, Vinet M, Balestro F, Meunier T, Urdampilleta M. Parity and singlet-triplet high-fidelity readout in a silicon double quantum dot at 0.5 K. PRX Quantum. 2022;3:040335.
66. Seedhouse AE, Tanttu T, Leon RC, Zhao R, Tan KY, Hensen B, Hudson FE, Itoh KM, Yoneda J, Yang CH, Morello A, Laucht A, Coppersmith SN, Saraiva A, Dzurak AS. Pauli blockade in silicon quantum dots with spin-orbit control. PRX Quantum. 2021;2:010303.
67. Hendrickx NW, Lawrie WIL, Russ M, van Riggelen F, de Snoo SL, Schouten RN, Sammak A, Scappucci G, Veldhorst M. A four-qubit germanium quantum processor. Nature. 2021;591:580.
68. Green TJ, Sastrawan J, Uys H, Biercuk MJ. Arbitrary quantum control of qubits in the presence of universal noise. New J Phys. 2013;15:095004.
69. Sivak DA, Crooks GE. Thermodynamic metrics and optimal paths. Phys Rev Lett. 2012;108:190602.
70. Xiao D, Chang M-C, Niu Q. Berry phase effects on electronic properties. Rev Mod Phys. 2010;82:1959.
71. Alvarez-Jimenez J, Dector A, Vergara JD. Quantum information metric and Berry curvature from a Lagrangian approach. J High Energy Phys. 2017;2017:44.
72. Gianfrate A, Bleu O, Dominici L, Ardizzone V, De Giorgi M, Ballarini D, Lerario G, West KW, Pfeiffer LN, Solnyshkov DD, Sanvitto D, Malpuech G. Measurement of the quantum geometric tensor and of the anomalous Hall drift. Nature. 2020;578:381.
73. Yu M, Yang P, Gong M, Cao Q, Lu Q, Liu H, Zhang S, Plenio MB, Jelezko F, Ozawa T, Goldman N, Cai J. Experimental measurement of the quantum geometric tensor using coupled qubits in diamond. Natl Sci Rev. 2020;7:254.
74. Motzoi F, Wilhelm FK. Improving frequency selection of driven pulses using derivative-based transition suppression. Phys Rev A. 2013;88:062318.
75. Ibáñez S, Chen X, Muga JG. Improving shortcuts to adiabaticity by iterative interaction pictures. Phys Rev A. 2013;87:043402.

76. Bukov M, Sels D, Polkovnikov A. Geometric speed limit of accessible many-body state preparation. Phys Rev X. 2019;9:011034.
77. Chen J-F. Speeding up quantum adiabatic processes with a dynamical quantum geometric tensor. Phys Rev Res. 2022;4:023252.
78. Tomka M, Souza T, Rosenberg S, Polkovnikov A. Geodesic paths for quantum many-body systems. 2016. arXiv:1606.05890.
79. Martinis JM, Geller MR. Fast adiabatic qubit gates using only σ z control. Phys Rev A. 2014;90:022307.
80. Cerfontaine P, Hangleiter T, Bluhm H. Filter functions for quantum processes under correlated noise. Phys Rev Lett. 2021;127:170403.
81. Hansen I, Seedhouse AE, Saraiva A, Dzurak AS, Yang CH. Accessing the full capabilities of filter functions: tool for detailed noise and quantum control susceptibility analysis. Phys Rev A. 2023;108:012426.
82. Polizzi E. FEAST eigenvalue solver v4.0 user guide. 2020. arXiv:2002.04807.
83. Zhang X, Morozova E, Rimbach-Russ M, Jirovec D, Hsiao T-K, Fariña PC, Wang C-A, Oosterhout SD, Sammak A, Scappucci G, Veldhorst M, Vandersypen LMK. Universal control of four singlet–triplet qubits. Nat Nanotechnol. 2024;1.
84. Jirovec D, Mutter PM, Hofmann A, Crippa A, Rychetsky M, Craig DL, Kukucka J, Martins F, Ballabio A, Ares N, Chrastina D, Isella G, Burkard G, Katsaros G. Dynamics of hole singlet-triplet qubits with large *g*-factor differences. Phys Rev Lett. 2022;128:126803.
85. Jirovec D, Hofmann A, Ballabio A, Mutter PM, Tavani G, Botifoll M, Crippa A, Kukucka J, Sagi O, Martins F, Saez-Mollejo J, Prieto I, Borovkov M, Arbiol J, Chrastina D, Isella G, Katsaros G. A singlet-triplet hole spin qubit in planar Ge. Nat Mater. 2021;20:1106.
86. Wang X, Bishop LS, Kestner JP, Barnes E, Sun K, Das Sarma S. Composite pulses for robust universal control of singlet–triplet qubits. Nat Commun. 2012;3:997.
87. Saez-Mollejo J, Jirovec D, Schell Y, Kukucka J, Calcaterra S, Chrastina D, Isella G, Rimbach-Russ M, Bosco S, Katsaros G. Exchange anisotropies in microwave-driven singlet-triplet qubits. Nat Commun. 2025;16:3862.
88. Geyer S, Hetényi B, Bosco S, Camenzind LC, Eggli RS, Fuhrer A, Loss D, Warburton RJ, Zumbühl DM, Kuhlmann AV. Anisotropic exchange interaction of two hole-spin qubits. Nat Phys. 2024;20:1152.
89. Ungerer JH, Pally A, Kononov A, Lehmann S, Ridderbos J, Potts PP, Thelander C, Dick KA, Maisi VF, Scarlino P, Baumgartner A, Schönenberger C. Strong coupling between a microwave photon and a singlet-triplet qubit. Nat Commun. 2024;15:1068.
90. van Riggelen-Doelman F, Wang C-A, de Snoo SL, Lawrie WIL, Hendrickx NW, Rimbach-Russ M, Sammak A, Scappucci G, Déprez C, Veldhorst M. Coherent spin qubit shuttling through germanium quantum dots. Nat Commun. 2024;15:1.
91. van Riggelen F, Lawrie WIL, Russ M, Hendrickx NW, Sammak A, Rispler M, Terhal BM, Scappucci G, Veldhorst M. Phase flip code with semiconductor spin qubits. npj Quantum Inf. 2022;8:1.
92. Bosco S, Scarlino P, Klinovaja J, Loss D. Fully tunable longitudinal spin-photon interactions in Si and Ge quantum dots. Phys Rev Lett. 2022;129:066801.
93. Hsiao T-K, Cova Fariña P, Oosterhout SD, Jirovec D, Zhang X, van Diepen CJ, Lawrie WIL, Wang C-A, Sammak A, Scappucci G, Veldhorst M, Demler E, Vandersypen LMK. Exciton transport in a germanium quantum dot ladder. Phys Rev X. 2024;14:011048.
94. Geyer S, Hetényi B, Bosco S, Camenzind LC, Eggli RS, Fuhrer A, Loss D, Warburton RJ, Zumbühl DM, Kuhlmann AV. Anisotropic exchange interaction of two hole-spin qubits. Nat Phys. 2024;20:1152.
95. Takeda K, Noiri A, Nakajima T, Kobayashi T, Tarucha S. Quantum error correction with silicon spin qubits. Nature. 2022;608:682.
96. Xue X, Russ M, Samkharadze N, Undseth B, Sammak A, Scappucci G, Vandersypen LMK. Quantum logic with spin qubits crossing the surface code threshold. Nature. 2022;601:343.
97. De Smet M, Matsumoto Y, Zwerver A-MJ, Tryputen L, de Snoo SL, Amitonov SV, Sammak A, Samkharadze N, Gül Ö, Wasserman RNM, Rimbach-Russ M, Scappucci G, Vandersypen LMK. High-fidelity single-spin shuttling in silicon. Nat Nanotechnol. 2025;20:866.
98. Paladino E, Galperin YM, Falci G, Altshuler BL. 1/f noise: implications for solid-state quantum information. Rev Mod Phys. 2014;86:361.
99. Yoneda J, Takeda K, Otsuka T, Nakajima T, Delbecq MR, Allison G, Honda T, Kodera T, Oda S, Hoshi Y, Usami N, Itoh KM, Tarucha S. A quantum-dot spin qubit with coherence limited by charge noise and fidelity higher than 99.9%. Nat Nanotechnol. 2018;13:102.
100. Kogan Sh. Electronic noise and fluctuations in solids. Cambridge: Cambridge University Press; 1996.
101. Zou J, Bosco S, Loss D. Spatially correlated classical and quantum noise in driven qubits. npj Quantum Inf. 2024;10:1.
102. Dutta P, Horn PM. Low-frequency fluctuations in solids: 1 f noise. Rev Mod Phys. 1981;53:497.
103. Burin AL, Shklovskii BI, Kozub VI, Galperin YM, Vinokur V. Many electron theory of 1/*f* noise in hopping conductivity. Phys Rev B. 2006;74:075205.
104. Krzywda JA, Cywiński Ł. Decoherence of electron spin qubit during transfer between two semiconductor quantum dots at low magnetic fields. Phys Rev B. 2025;111:115305.
105. MacQuarrie ER, Neyens SF, Dodson JP, Corrigan J, Thorgrimsson B, Holman N, Palma M, Edge LF, Friesen M, Coppersmith SN, Eriksson MA. Progress toward a capacitively mediated CNOT between two charge qubits in Si/SiGe. npj Quantum Inf. 2020;6:1.
106. Hu C-K, Santos AC, Cui J-M, Huang Y-F, Sarandy MS, Li C-F, Guo G-C. Adiabatic quantum dynamics under decoherence in a controllable trapped-ion setup. Phys Rev A. 2019;99:062320.
107. Santos AC, Villas-Boas CJ, Bachelard R. Quantum adiabatic brachistochrone for open systems. Phys Rev A. 2021;103:012206.
108. Hou X-Y, Zhou Z, Wang X, Guo H, Chien C-C. Local geometry and quantum geometric tensor of mixed states. Phys Rev B. 2024;110:035144.
109. Hörnedal N, Prośniak OA, del Campo A, Chenu A. A geometrical description of non-Hermitian dynamics: speed limits in finite rank density operators. Quantum. 2025;9:1729.

110. Lewis D, Wiersema R, Bose S. Quantum optimal control with geodesic pulse engineering. 2025. arXiv:2508.16029.
111. Vandermause J, Ramanathan C. Superadiabatic control of quantum operations. Phys Rev A. 2016;93:052329.
112. Larocca M, Wisniacki D. Krylov-subspace approach for the efficient control of quantum many-body dynamics. Phys Rev A. 2021;103:023107.

Publisher's note